AFRL-AFOSR-JP-TR-2019-0061

Effects of Wall Temperature in High Enthalpy Rarefied Hypersonic Separated Flow

Sudhir Gai
University of New South Wales-NEW NCAGE Code
HIGH STREET
KENSINGTON, NSW, 2052
AU

10/10/2019
Final Report

Air Force Research Laboratory
Air Force Office of Scientific Research
Asian Office of Aerospace Research and Development
Unit 45002, APO AP 96338-5002

REPORT DOCUMENTATION PAGE

Form Approved
OMB No. 0704-0188

1. REPORT DATE *(DD-MM-YYYY)*	2. REPORT TYPE	3. DATES COVERED *(From - To)*
10-10-2019	Final	24 Jun 2016 to 23 Jun 2018

4. TITLE AND SUBTITLE
Effects of Wall Temperature in High Enthalpy Rarefied Hypersonic Separated Flow

5a. CONTRACT NUMBER

5b. GRANT NUMBER
FA2386-16-1-4014

5c. PROGRAM ELEMENT NUMBER
61102F

6. AUTHOR(S)
Sudhir Gai

5d. PROJECT NUMBER

5e. TASK NUMBER

5f. WORK UNIT NUMBER

7. PERFORMING ORGANIZATION NAME(S) AND ADDRESS(ES)
University of New South Wales-NEW NCAGE Code
HIGH STREET
KENSINGTON, NSW, 2052 AU

8. PERFORMING ORGANIZATION REPORT NUMBER

9. SPONSORING/MONITORING AGENCY NAME(S) AND ADDRESS(ES)
AOARD
UNIT 45002
APO AP 96338-5002

10. SPONSOR/MONITOR'S ACRONYM(S)
AFRL/AFOSR IOA

11. SPONSOR/MONITOR'S REPORT NUMBER(S)
AFRL-AFOSR-JP-TR-2019-0061

12. DISTRIBUTION/AVAILABILITY STATEMENT
A DISTRIBUTION UNLIMITED: PB Public Release

13. SUPPLEMENTARY NOTES

14. ABSTRACT
The initial goals of the project were to investigate the behavior of high to moderate enthalpy rarefied hypersonic flow in a strong thermal non-equilibrium for wall temperature conditions of 300K and 1500K. Due to complexity, the highest wall temperature used was 800K. Nonetheless, this research represents, for the first time, shock tunnel experiments on a large separated hypersonic rarefied flow with a heated wall up to 800K that yielded a wall to stagnation temperature of ratio of 0.25. The experimental surface of the model was made of graphite and the experiments were conducted on a large separated flow at hypersonic conditions in free-piston driven shock tunnel at an enthalpy of 3.1 MJ/kg, Reynolds number of 1.34 x 10^6 m^-1 and a Mach number of 10. Analysis and simulations, both Navier-Stokes and DSMC have shown that both primary and secondary separations are strongly influenced by the wall temperature. The results of the experiments showed reasonable agreement with numerical data and provided confidence that future work with higher temperatures is feasible using a simpler configuration. Higher temperature experiments can provide important data for modeling and design of space vehicles.

15. SUBJECT TERMS
AOARD, Nonequilibrium flows, hypersonic

16. SECURITY CLASSIFICATION OF:			17. LIMITATION OF ABSTRACT	18. NUMBER OF PAGES	19a. NAME OF RESPONSIBLE PERSON
a. REPORT	b. ABSTRACT	c. THIS PAGE			SINGLETON, BRIANA
Unclassified	Unclassified	Unclassified	SAR		19b. TELEPHONE NUMBER *(Include area code)* 315-227-7007

Standard Form 298 (Rev. 8/98)
Prescribed by ANSI Std. Z39.18

Effects of Wall Temperature in High Enthalpy Rarefied Hypersonic Separated Flow

Grant Number: **FA2386-16-1-4014**

Final Report with Results from Experiments in a Shock Tunnel

Sudhir Gai, Andrew Neely, and Harald Kleine

Collaborators: Liam McQuellin, Gaetano Currao, and Amna Khraibut

UNSW Canberra

24 September, 2018

UNSW CANBERRA

Effects of Wall Temperature in High Enthalpy Rarefied Hypersonic Separated Flow

Final Report with Results from Experiments in a Shock Tunnel

Grant Number: FA2386-16-4024

Sudhir Gai, Andrew Neely, and Harald Kleine

Collaborators: Liam McQuellin, Gaetano Currao, and Amna Khraibut

UNSW Canberra

24 September, 2018

Abstract

This Report presents, for the first time, shock tunnel experiments on a large separated hypersonic rarefied flow with a heated wall up to 800K. The experimental surface of the model was made of graphite and the design included some unique features, which are detailed in the Report. Although the graphite surface sustained repeated damage during the experiments and needed to be replaced, useful data has been obtained which compared very favourably with numerical simulations.

Introduction

Our earlier theoretical and numerical studies, both Navier-Stokes CFD (Khraibut *et al.* 2017) and DSMC (Prakash *et al.* 2018) suggested that a large-scale separated flow, such as the leading edge separation, is characterised by a main recirculating region and a small secondary vortex (the so called Moffatt eddy) embedded within it. In Khraibut *et al.* (2017) study, it was found that wall temperature has a strong effect on both the main vortex as well as the secondary vortex. This study showed that as the wall temperature increased from 300 K (baseline value) to 800 K, and then to adiabatic value, there was a shift of both main and secondary vortex downstream. With a cold wall of 300 K, the secondary vortex was disposed largely asymmetrically on the expansion surface, while the main vortex was centred towards the compression surface (Figure 1). With increase in temperature to 800 K, both the secondary and the main vortex were displaced downstream, the secondary vortex being nearly symmetrical with respect to the corner vertex (Figure 2). In the limiting adiabatic wall case, both the secondary and the main vortex had moved sufficiently downstream such that both were now completely on the compression surface (Figure 3).

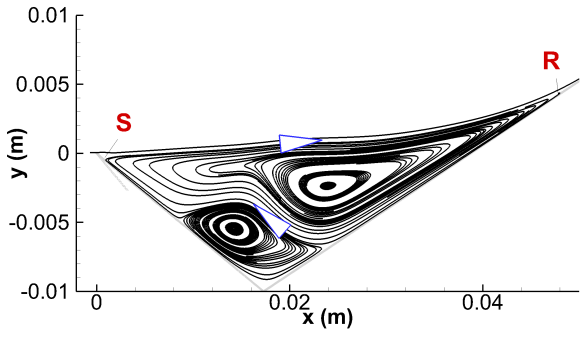

Figure 1: Streamlines in leading edge separation (Tw = 300 K).

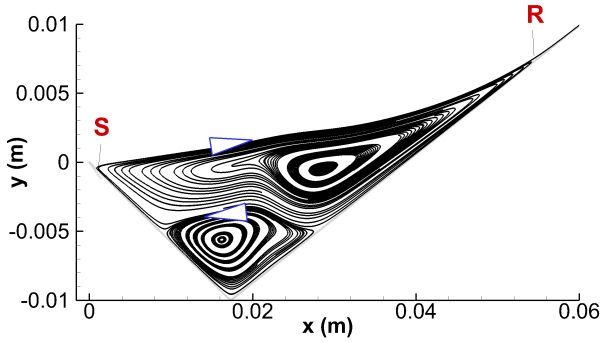

Figure 2: Streamlines in leading edge separation (Tw = 800 K).

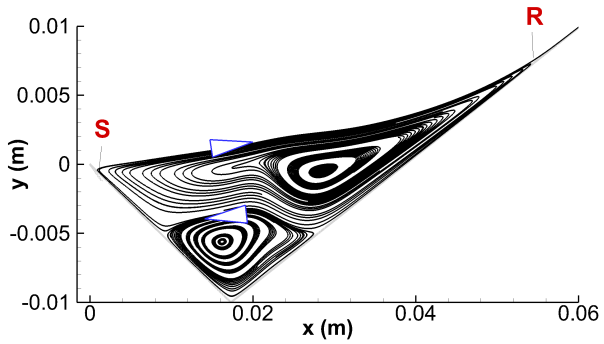

Figure 3: Streamlines in leading edge separation (Tw = 2770 K).

It was also found (Prakash *et al.* 2018; Tumuklu *et al.* 2017) that the formation and enlargement of the secondary vortex is a time-dependent phenomenon and that it takes several milliseconds (typically 2 to 4 milliseconds) to achieve steady state. Such long flow times are not achievable in our T-ADFA shock tunnel, which has a total test time of the order of 1.5 ms. Nevertheless, our DSMC computations (Prakash *et al.* 2018) have shown that by 1.5 ms, the secondary vortex has grown to its full size but is still largely on the expansion surface, having yet not reached steady state. It is also not symmetrically disposed with respect to the corner as in the case of Navier-Stokes simulations of Khraibut *et al.* (2017). It should be pointed out that the steady state solution of Khraibut *et al.* (2017) at 300 K agree with the steady state solution of Tumuklu *et al.* (2017) when their DSMC solutions were continued up to 2.6 ms.

In the light of these observations and as there is no data at all on any hot wall separated flows, it was thought worthwhile to investigate the hot wall effects on our leading edge separation model ('Tick model)'. A temperature of 800 K was chosen as there is data available to compare the results with. Moreover, 800 K was the maximum possible with our available power and equipment.

The following sections will describe the model design, equipment, and tests. The conclusions and recommendations for future work are then outlined.

Mechanical Design of the Model

Thermal structural design of heated tick model

The first phase of the project had shown that C/SiC was the ideal material for use as a resistive heater in a wind tunnel model (Vennik *et al.* 2017), given its high strength and high resistivity, but it also proved to be prohibitively expensive and hard to machine (Schnitzer 2017). Therefore, specialist grade graphite was sourced from Thermic Edge in the UK for the heater plates for the tic model. Graphite was selected due to its high electrical resistance, its relative machinability and its cost. It had also been successfully used in Phase 1 when the original C/SiC was fractured (Schnitzer 2017).

Two grades of graphite were selected for use (Table 1). SPG45 (high electrical resistivity) was chosen for the compression surface heater as it would allow the highest temperature rise for the available power, given that the size of this plate would constrain the ability to heat it. SPG60 (Ultra fine grained high expansion) was chosen for the expansion surface due to its high flexural strength, at the cost of a slight decrease in resistivity, as this smaller heater was not constrained by power but was subject to the highest aerodynamic loads (on the underside of the leading edge) and could not be reinforced.

Table 1. Material properties for Specialist Graphite Grades from Thermic Edge (REF). Selected materials are highlighted in blue.

Main Characteristic	Densified	High thermal conductivity	High electrical reststivity	High strength & expansion	High strength & expansion densified	Ultra fine grained high expansion
Grade	SPG35	SPG40	SPG45	SPG50	SPG55	SPG60
Average grain size-microns	13	10	5	4	4	<1
Density - g/cc	1.88	1.82	1.65	1.77	1.77	1.79
Porosity- %	4%	10%	25%	20%	4%	20%
Thermal Conductivity-W/mK	111	140	75	95	95	72
CTE-microns/m.degC	5	4.8	7.7	8.1	8.1	8.1
Flexural Strength- Mpa	57	54	53	85	85	110
Compressive Strength-Mpa	126	90	105	140	140	195
Youngs Modulus - Gpa	12.6	11	9	11	11	14.5
Shore Hardness	65	55	68	74	74	85
Resistivity- uOhm cm	1170	900	1900	1500	1500	1750
Max operating temp- in air	500 deg C	500 deg C	500 deg C	500 deg C	500 deg C	500 deg C
-in vacuum	2200 degC	2200 degC	2200 degC	2200 degC	2200 degC	2200 degC
-in innert gas	2000 degC	2000 degC	2000 degC	2000 degC	2000 degC	2000 degC

Structural modelling of the ceramic heater plates was performed using the FEM solver in ANSYS Workbench to

1) Achieve suitable operating temperatures and heat up times
2) Ensure that the heated plates (particularly the leading edge) were not structurally overload by the flow.

Numerical heating studies

The thermal module of the ANSYS FEM solver was used to establish the required geometries of the graphite heater plates to ensure suitable operating temperatures and heat up times (Figure 4). A range of heater powers, planforms and plate thicknesses were examined. Radiative loss to the ambient surroundings was included in the calculations but free convective loss was not as the experiments are performed in a vacuum and the hypersonic test flow is actually convectively heating the surfaces although the resulting temperature rises are expected to be insignificant due to the short duration of the flow and to the reduced driving temperature difference when the model is resistively heated.

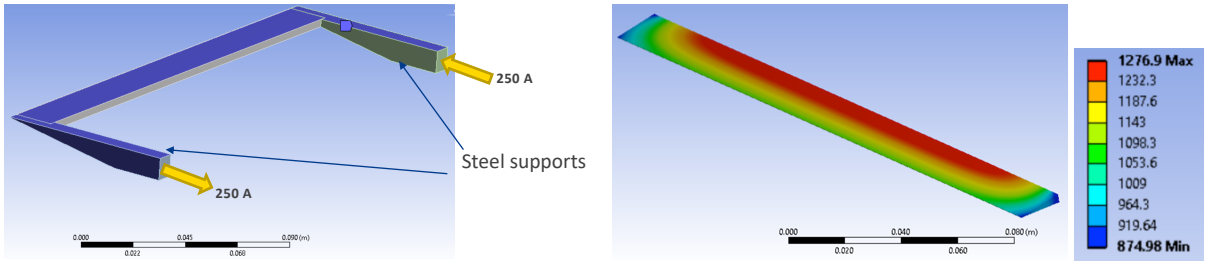

Figure 4. Thermal-electric model for the graphite expansion surface and steel bus bars.

Figure 5 shows the predicted temperature distribution on the surface of the graphite heater plates for the final design with the expansion and compression heaters running on separate curcuits at different powers.

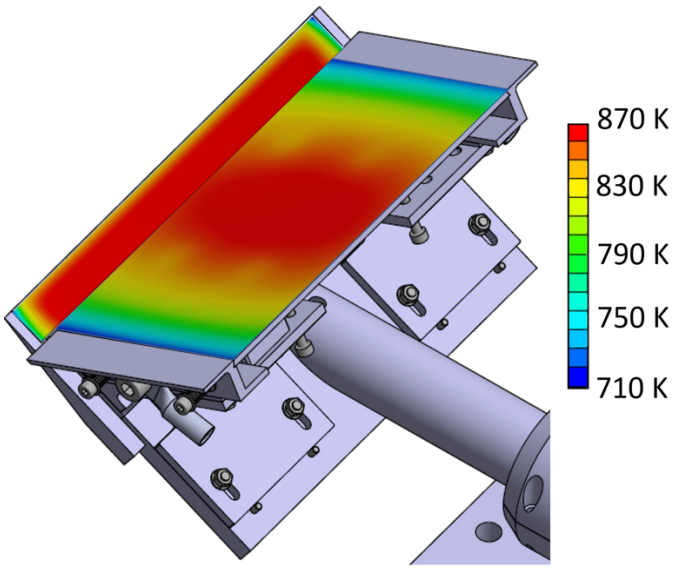

Figure 5. Surface temperature distribution on the model from FEM thermal-electric model. (Expansion surface 1-2 s to reach 800K at 250 A, compression surface 50 s to reach 800K at 450 A)

Figure 6 shows the predicted spanwise temperature distributions across both the expansion and the compression surfaces. It can be seen that the two dimensionality of the temperature distribution is within 1 K on the expansion surface and within 5 K for the middle 1/5th of the compression surface. The spanwise nonuniformity is due to the heat capacity of the busbars and the resultant thermal conduction back into them, cooling the edges of the heater plate. This is less severe in the expansion surface heater due to the lower thermal mass in close proximity to the heater. The axial gradient in the expansion surface heater is due to the nonuniform spanwise cross section of this heater. The balance between radiative loss from the surface and internal Joule heating incrases with the ratio of surface area to internal volume toward the sharp leading edge, colling the tip of the heater plate.

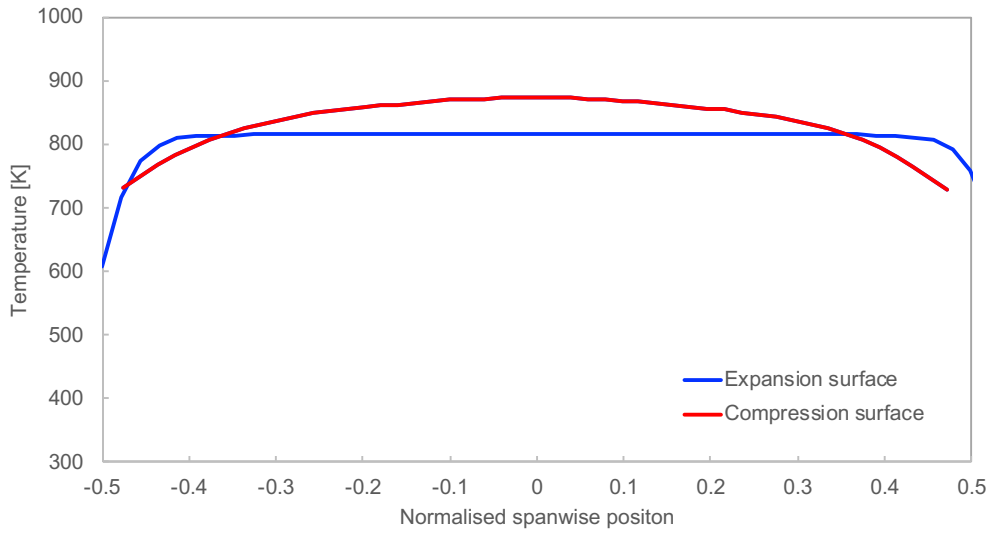

Figure 6. Span-wise temperature distributions for the expansion and compression surfaces predicted from FEM simulations.

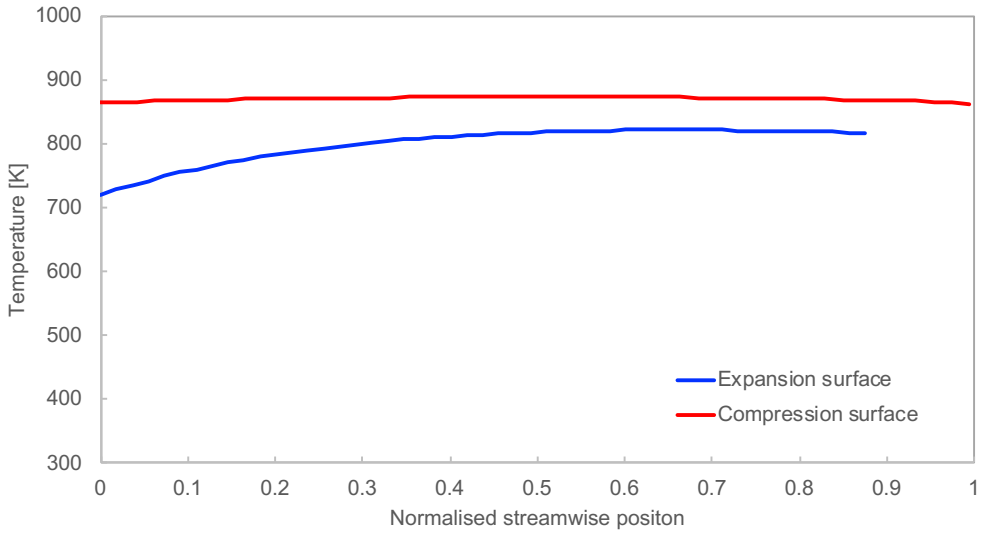

Figure 7. Stream-wise temperature distributions for the expansion and compression surfaces predicted from FEM simulations.

Flow loading of the heated plates

A thermal-structural analysis of the heater plates was also performed to confirm that the plates would not deflect significantly or fail under the aerodynamic loads during the test flow. The pressure distributions measured by Khraibut *et al.* (2017) were applied to the surface of the model to calculate the distributions of stress and deformation in the graphite heater plates (Figure 8).

One consequence of this study was that a set of four insulated supports, machined from alumina, where added to the design to reduce the unsupported area of the compression plate. Distributions of the resulting stress fields in the graphite heater plates are shown in(Figure 8). The predicted peak stresses were safely below the flexural strength of the graphite (53 MPa for the expansion surface) with the circular supports in place, even when accounting for the impulsive loading (Figure 8).

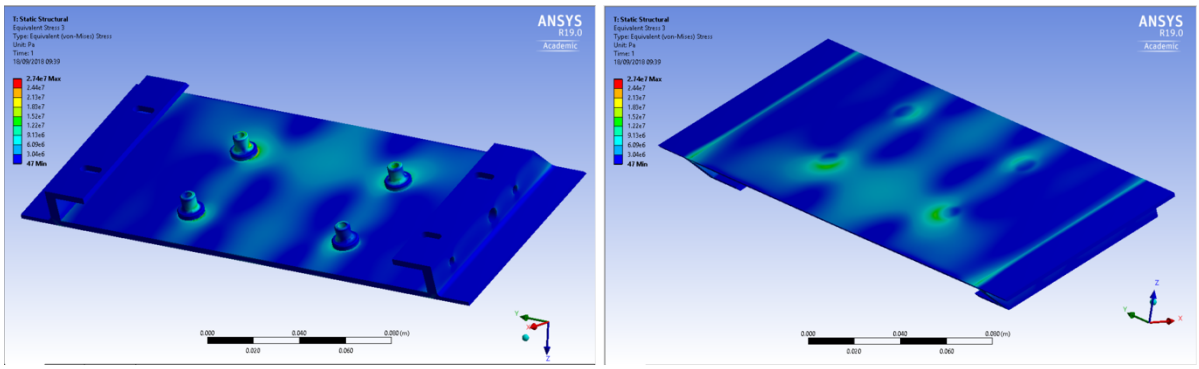

Figure 8. Stress distributions in graphite heater plate forming the compression surface. The peak stresses are safely below the flexural strength of the graphite (53 MPa). (a) underside of the plate showing the alumina supports, (b) windward surface.

Detailed design of the heated tick model

The experimental model was designed such that geometric features remained similar to those described during previous studies (Prakash, Gai, & O'Byrne, 2018). A large portion of mechanical elements from the existing 'tick' model were utilised as these components had been proven to be suitable for experiments within the T-ADFA facility. This also reduced the number of components which required manufacturing. Figure 9 depicts a top and side view of the model, indicating the major dimensions.

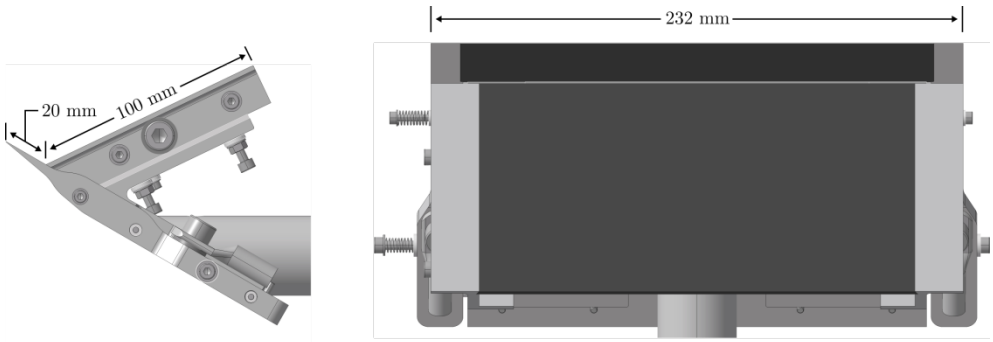

Figure 9 - Hot Wall Model two-view

The re-compression surface, previous manufactured from Aluminium alloy, was replaced with a graphite resistive element, and steel bus-bars. While the re-compression surface remained 100 mm in length, the width was increased from 200mm to 232 mm, resulting in an aspect ratio of 2.32. 190mm of this width consisted of the resistive heater, which, as shown in Figure 10, was supported in place by two bus-bars (Bus-Bar A & B). The graphite re-compression surface consisted of a 3 mm thick, linished graphite panel, which incorporated machined features where the panel interfaced with the bus bars. A 25° bevel on the edges, with a 0.2 mm fillet applied to the resulting sharp edge, forms the bus-bar interface. This allowed the panel to be constrained from movement in the vertical direction. To provide sufficient mechanical clamping of the panel, whilst ensuring a low-resistance electrical connection, a technique utilising compression springs was incorporated. This technique was first devised by [Jai thesis] and then further improved in [Mario thesis]. The graphite panel upon heating, would result in panel expansion. This expansion force is counteracted by the compression spring, which enables the model to expand in the transverse direction, whilst maintaining sufficient holding force and maintaining an electrical connection.

During the design process, it was determined that in order to reach the desired wall temperature (800 K), whilst maintaining a nominally uniform temperature profile, both the expansion and re-compression surfaces were required to be energised independently. This is a result of the difference in resistance (a function of cross-sectional area. A single heating element, while technically possible, would require a large graphite blank, and significant machining operations to produce the required geometry and supporting infrastructure.

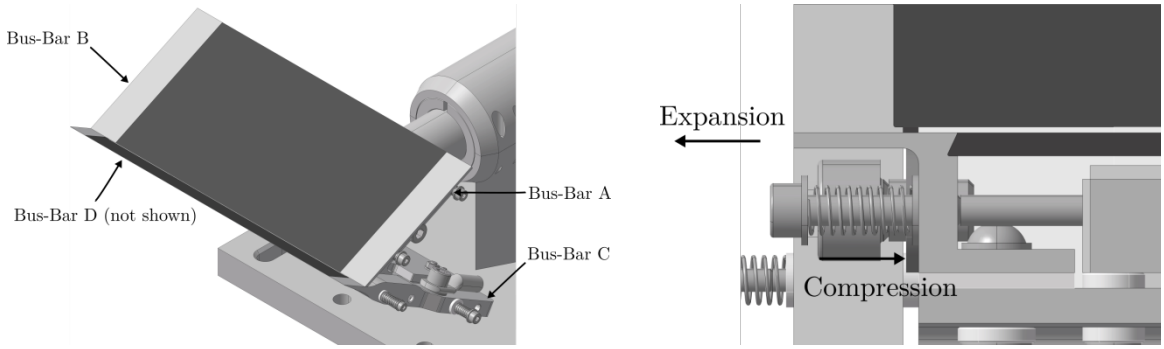

Figure 10 - Detail of Bus-bar arrangement

Bus-bar B was fixed in place, while bus-bar A was allowed to translate in the span-wise direction. Compression force was adjusted using two M4 fasteners, spaced symmetrically about the centreline of the bus-bar. This allowed for asymmetric adjustment creating a uniform clamping arrangement. The non-threaded portion of the fastener also served as a means to constrain the bus bar from rotation. Exploded and assembled views of Bus-bar A can be seen in Figure 11.

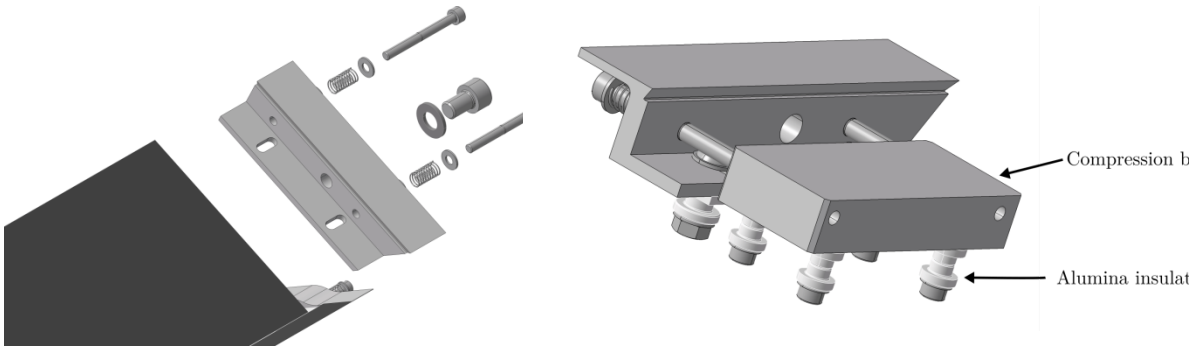

Figure 11 - Bus-Bar A compression arrangement

The heated expansion surface, which re-produced the 10° steel leading edge in the cold model, is depicted in Figure 12. The small angle leading edge, when manufactured from graphite, was subject to a finite achievable leading edge sharpness using conventional manufacturing techniques. The leading edge radius was fixed to 100 μm ± 15 μm. In order to conform to the method in which surfaces were modelled in numerical studies, the geometry was created to feature a 20 mm planar surface, with the leading edge radius extending from the tangent of the circle.

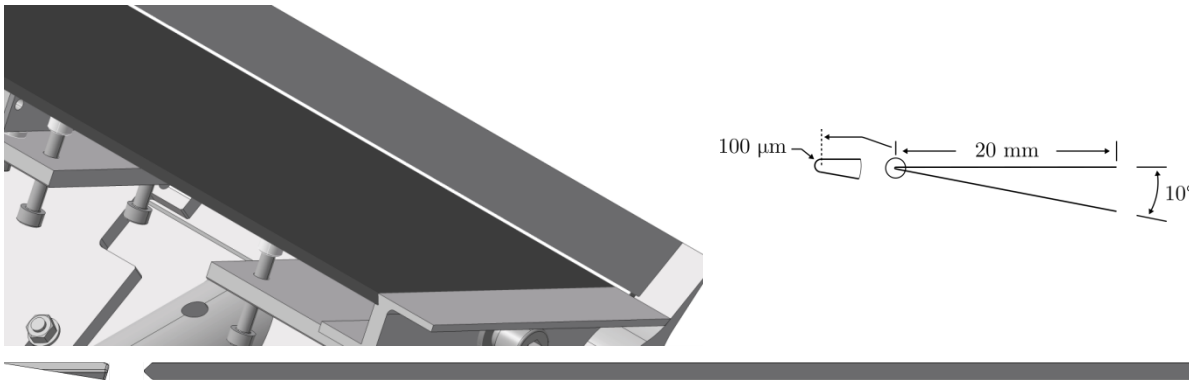

Figure 12 - Detail of expansion surface

Chamfers were placed on the upper and lower surfaces of the leading edge to provide a mechanism to constraint the leading edge within the bus-bar. Unlike the re-compression surface, the leading-edge graphite surface had to be self-supporting, but also, able to accommodate mechanical loading experienced during the flow duration. To accommodate such a complex geometry, the expansion surface bus-bars (Bus Bar C & D) were designed to support the leading edge using a pocket as seen in Figure 13.

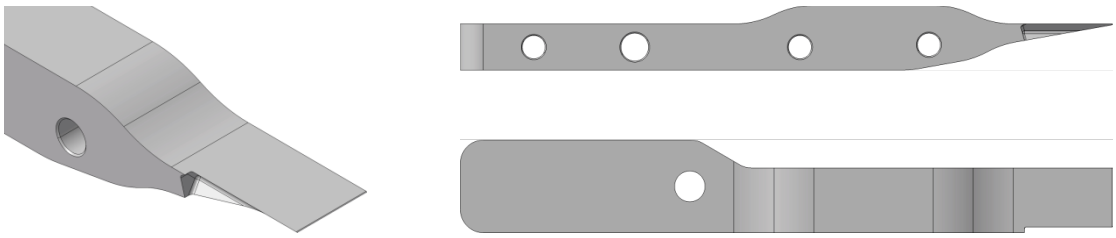

Figure 13 - Leading-edge Bus-Bar C

Like Bus-bar A, the leading-edge bus-bar (bus-bar C) is constrained to translate in the span-wise direction only. This was achieved using steel locating pins seated in Alumina 'hats' that electrically isolated the bus-bar from other mechanical elements of the model. Springs were also used to provide compression of the leading-edge, while maintaining a sufficient electrical connection. An exploded view of the bus-bar (C) arrangements can be seen in Figure 14.

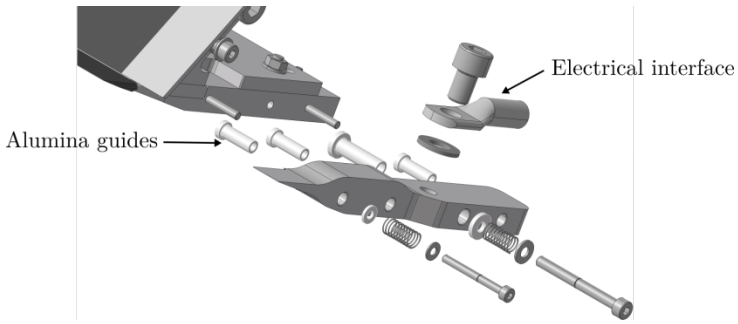

Figure 14 - Bus-bar C compression and insulation arrangement

Because the expansion and re-compression surfaces are separately excited, a form of isolation was required between the bus-bars and heated elements. Alumina was used to prevent the leading edge from coming in electrical contact with the remainder of the model, but still provided mechanical support. A steel clamp was used to constrain the alumina insulator.

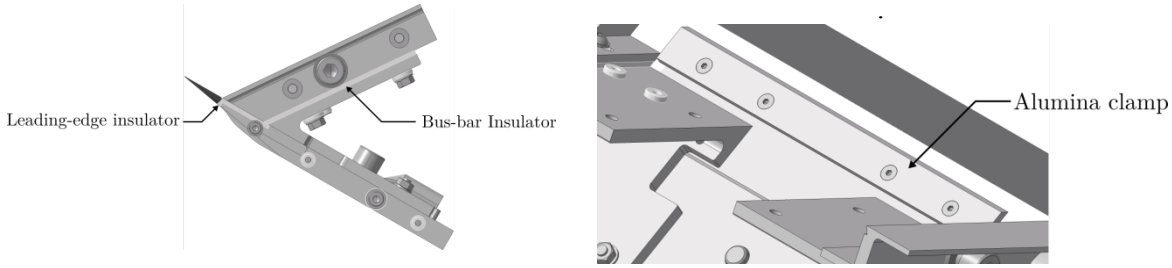

Figure 15 - Leading edge insulator and support clamp

The large aspect ratio and reduced thickness of the graphite re-compression surface left potential for the graphite to deform during the test time in T-ADFA. To minimise this, supports were placed on the leeward face of the graphite panel which minimised panel deformation.

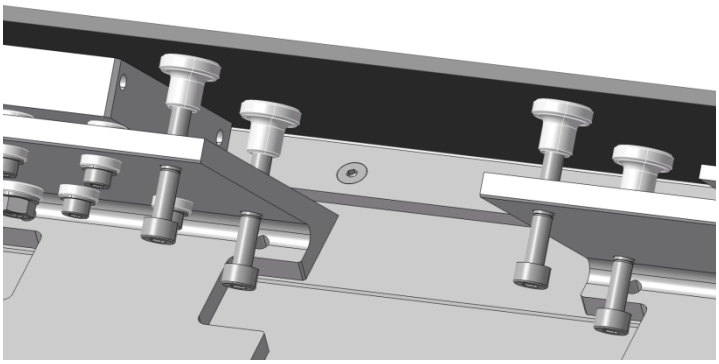

Figure 16 - Alumina rear supports for re-compression surface

The assembled model is shown in Figure 17. The model was assembled and first tested on the bench to establish the appropriate power settings for operation in the shock tunnel. The model was them moved to the T-ADFA laboratory and mounted in the shock tunnel test section where the heaters were again tested both in air and then in vacuum before being tested in the hypersonic flow.

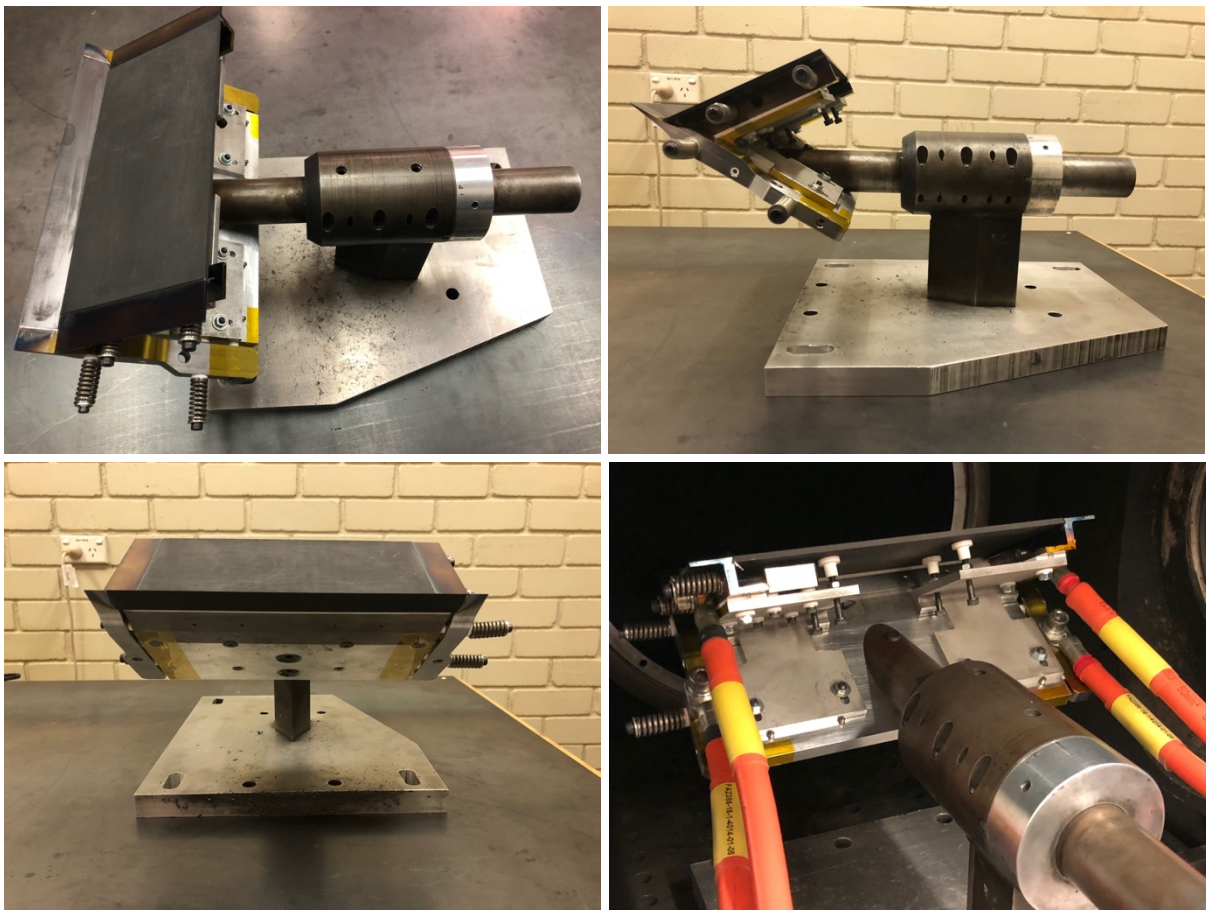

Figure 17. Multiple views of the assembled heated tick model with graphite resistive heaters for the expansion and compression surfaces. The rear view of the model, mounted in the tunnel, shows the detail of the alumina supports for the compression surface.

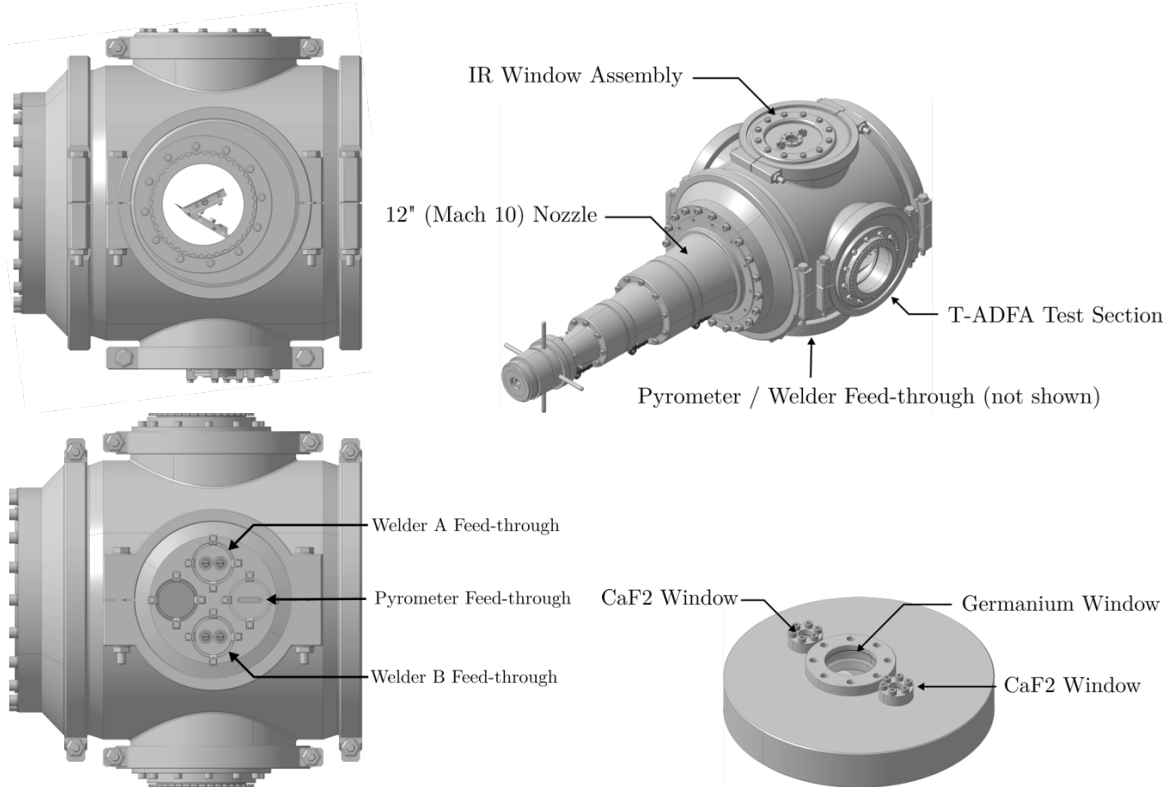

Figure 18. Detail of test section configuration (a) elevation with model, (b) underside showing instrumentation and power pass-throughs, (c) assembled test section with nozzle and (d) observation windows.

Instrumentation

The two primary forms of instrumentation for the experiment were visualisation of the flow field over the heated model and measurement of the surface temperature distribution over the heated tick model immediately before and after the test flow.

Flow Visualisation

The flow was visualised by means of a polychrome shearing interferometer (Merzkirch 1987, Kleine 2001) set up with two Wollaston prisms (shear angle 1') and two spherical mirrors (focal length 3 m). The system was set to infinite fringe width, with the shear being in the horizontal direction so that density gradients perpendicular to the flow direction were captured (Figure 19). The light source was a continuous 10 W LED and the images were recorded with a high-speed camera (Phantom 710, 15,000 frames per second, 66 ms exposure time, resolution 1024 x 400 pixel). The overall recording length was 2.8 s, which allowed one to capture the complete process of flow build-up, test time, and tunnel shutdown. The image magnification factor was 0.15. As a result of the low initial density level, higher order fringes (and thus different colours) are only seen in the region behind the oblique shock emanating from the tip to the lower part of the model.

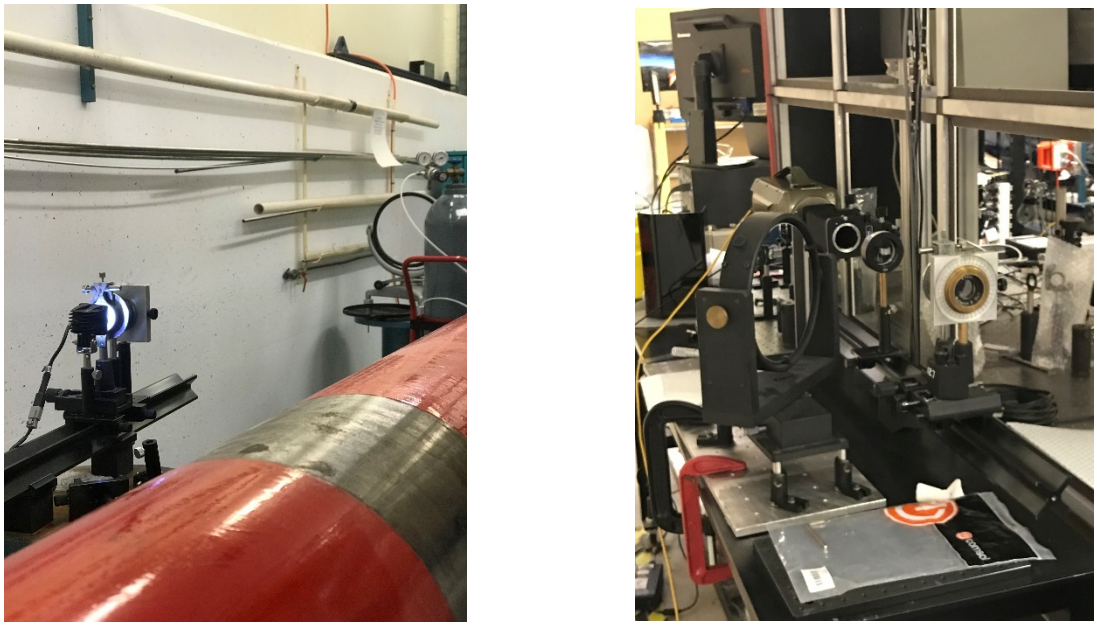

(a) (b)

Figure 19. Arrangement of polychrome shearing interferometer: (a) White light source; (b) highspeed camera.

Measurement of heater surface temperatures

Surface temperatures on the heated tick model were monitored using the combination of a long-wave IR thermographic camera (Micro-Epsilon TIM640), a two-colour, high-temperature pyrometer (LumaSense IGAR 12-LO) and a single colour low-temperature pyrometer (Micro-Epsilon thermoMETER CS).

The TIM640 IR camera (7.5 to 13 μm) was positioned above the test section and viewed the planform of the model (both the expansion and compression surfaces) through a germanium window. The LumaSense IGAR 12-LO two-colour pyrometer (1.52 and 1.64 μm) was used to measure a point on the expansion surface through an adjacent calcium fluoride window. As the IGAR 12-LO (MB10) can only measure temperatures in the range from 300 to 1000 °C, an additional low-temperature pyrometer (Micro-Epsilon thermoMETER CS) was mounted inside the test section to measure the temperature of a point on the compression surface.

The thermographic measurements were calibrated on the benchtop across the expected temperature range by adjusting the emissivity setting of the IR camera and the low-temperature pyrometer to match the temperature reported by the two-colour pyrometer at the same surface location. The IGAR 12-LO pyrometer provides a measurement independent of surface emissivity when operated in two-colour mode. The measurements were also performed through the windows to establish the transmission correction required for the material. In this way the temperature dependence of the emissivity of the surface of the heated graphite was determined for the experiments.

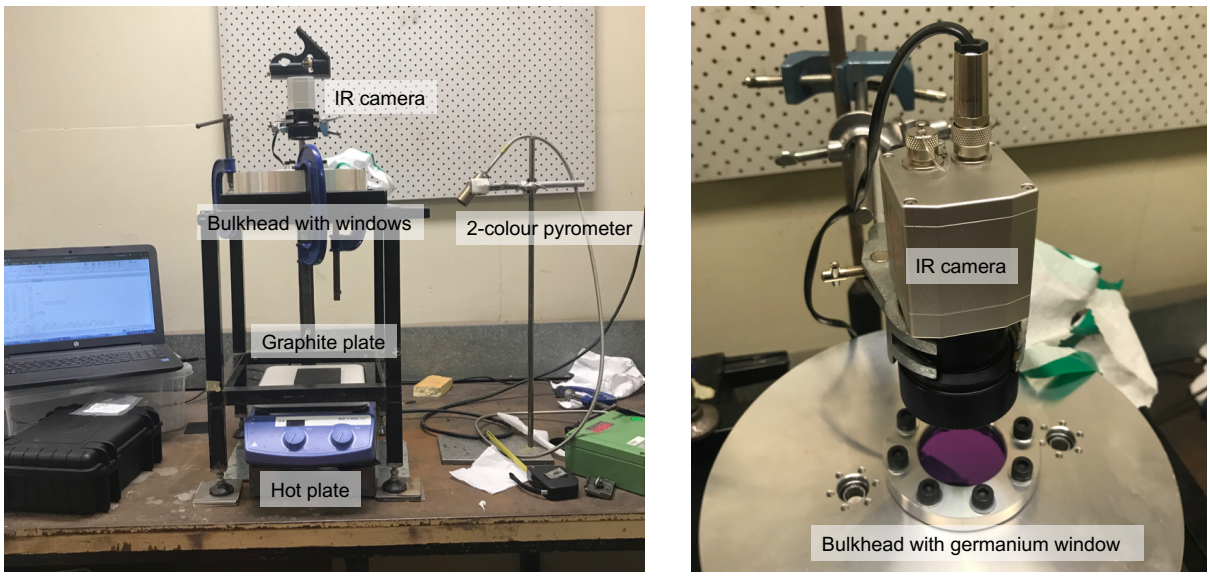

Figure 20. Benchtop calibration of the IR camera using hot plate (300 – 500 K)

The temperature of a graphite plate was measured for a range of temperatures on the hot plate. The temperature readings from the long-wave IR camera were adjusted by correcting the emissivity to match the value reported from the two-colour pyrometer. The measured dependence of these deduced values of emissivity are plotted in Figure 21. Unlike the data reported by Neuer and Jaroma-Weiland (1998) in Figure 22, these values show a slight dependence on temperature and are also lower, noting that the data from the literature was measured at significantly higher temperatures than those used in the benchtop calibration.

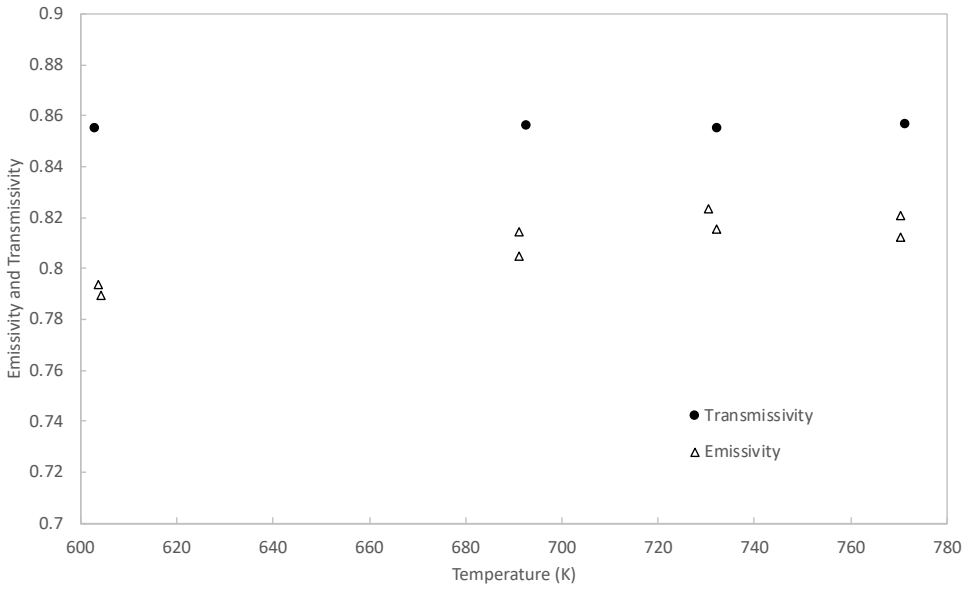

Figure 21. Emissivity of the graphite and transmissivity of the germanium window for a range of temperatures from the hot plate calibration tests performed on the benchtop.

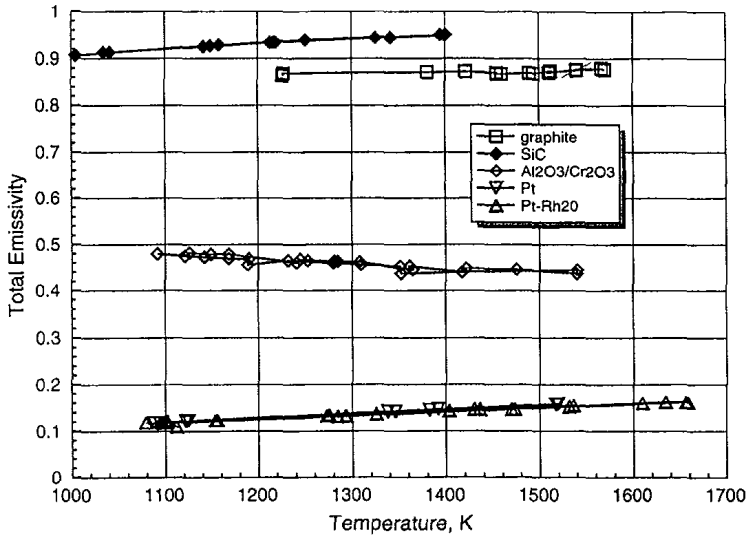

Figure 22. Total normal emissivity of various materials (Fig 11 from Neuer and Jaroma-Weiland 1998)

The transmissivity of the windows was calculated by comparing the surface temperature values measured through the window to those with the window removed. Values for the germanium window are shown in Figure 21 with an average transmissivity of 0.855, and compared with the manufacturer supplied values across a range of wavelengths in Figure 23.

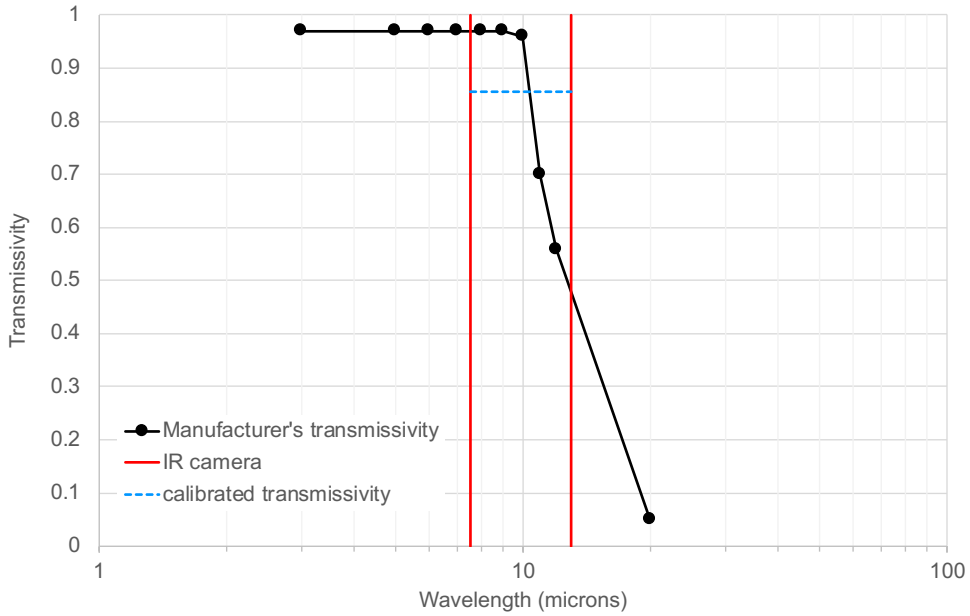

Figure 23. Transmissivity of the germanium window for the bandwidth of the IR camera.

Bench Testing of the Heated Tick Model

Bench testing of the assembled model was performed to examine the uniformity of heating and establish the heating times required to achieve the desired temperatures. Initial testing at lower temperatures showed that hot spots appeared at the interface of the graphite plate with the busbars but these were largely smeared out at the higher temperatures (Figure 24).

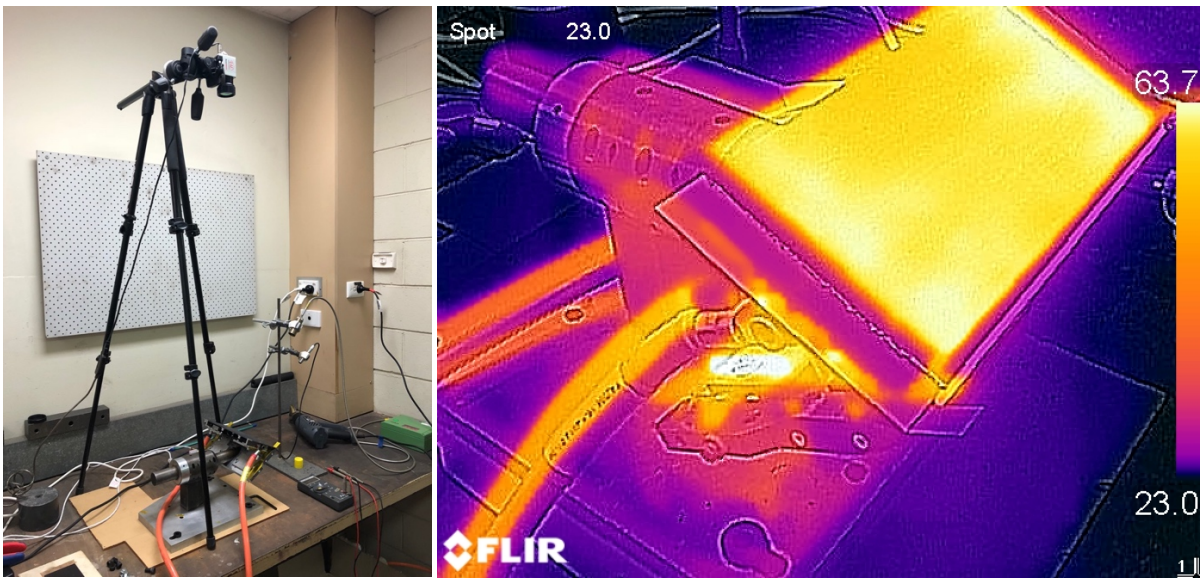

Figure 24. Bench testing of the compression plate heater. Expansion plate note attached.

Temperature distributions across the surface of the compression plate are shown in Figure 25. It can be seen that the axial and span-wise nonuniformity of temperature measured in the bench tests is close to that predicted by the FEM simulations. The localised variation of temperature observed is due to the nonuniformity of emissivity on the surface of the heater plate due to machining variations and depositions on the surface.

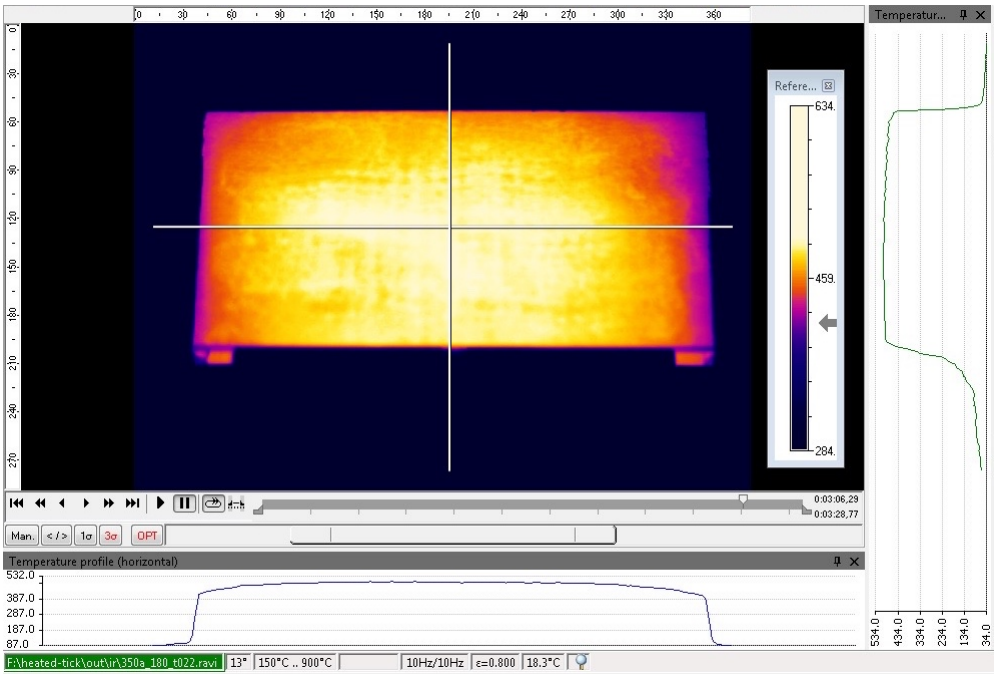

Figure 25. Temperature distribution (°C) across the compression surface measured during bench testing at 350 A supply current after 180 s.

As it was required to run the compression surface heater at full power (350 A setting) for 180 seconds to reach its radiation adiabatic wall temperature, bench testing was used to establish the required power setting for the expansion surface to reach a radiation adiabatic wall temperature of 800 K (Figure 26). It was established that a power supply setting of 62A was sufficient to heat the expansion surface to the required level in the same 180s required to heat the compression surface.

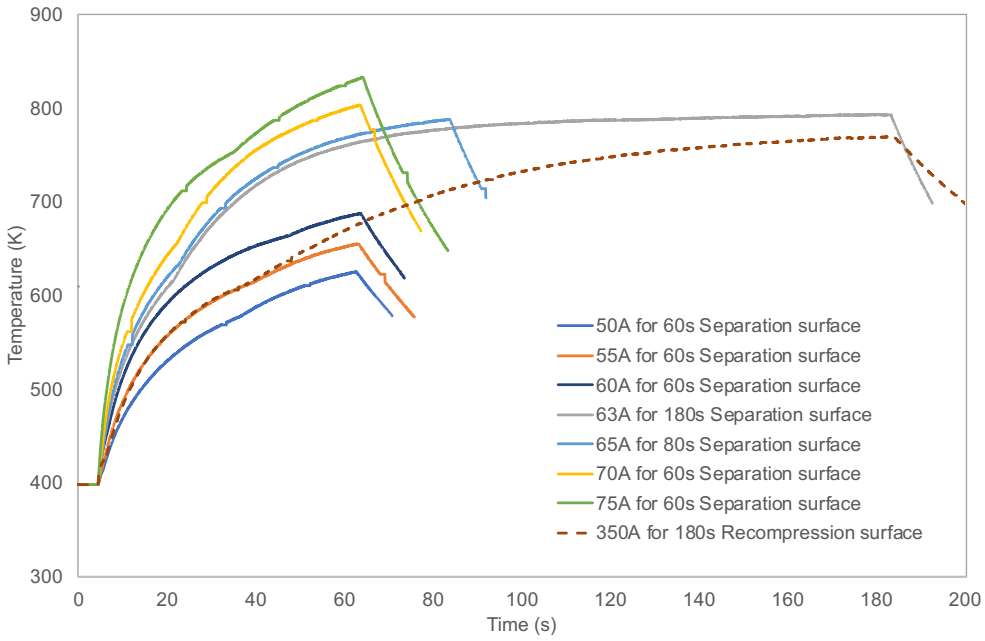

Figure 26. Temperature-time history for expansion and compression surfaces

Note that the heating times shown in Figure 26 are longer than those from the FEM shown in Figure 5 due to the lower heater power used (350A supply v a 450A supply).

Experimental Method

For the shock tunnel experiments, the assembled model was mounted in the T-ADFA test section (Figure 27). The compression surface was viewed from above by the IR camera positioned outside the tunnel. The temperature at the centre of the expansion surface was measured by the two-colour pyrometer, through the calcium fluoride window, located directly above the model. The temperature of the compression surface was also measured during heat-up and cool-down using the low temperature pyrometer, mounted inside the test section above the nozzle, facing downstream. Figure 28 shows the arrangement.

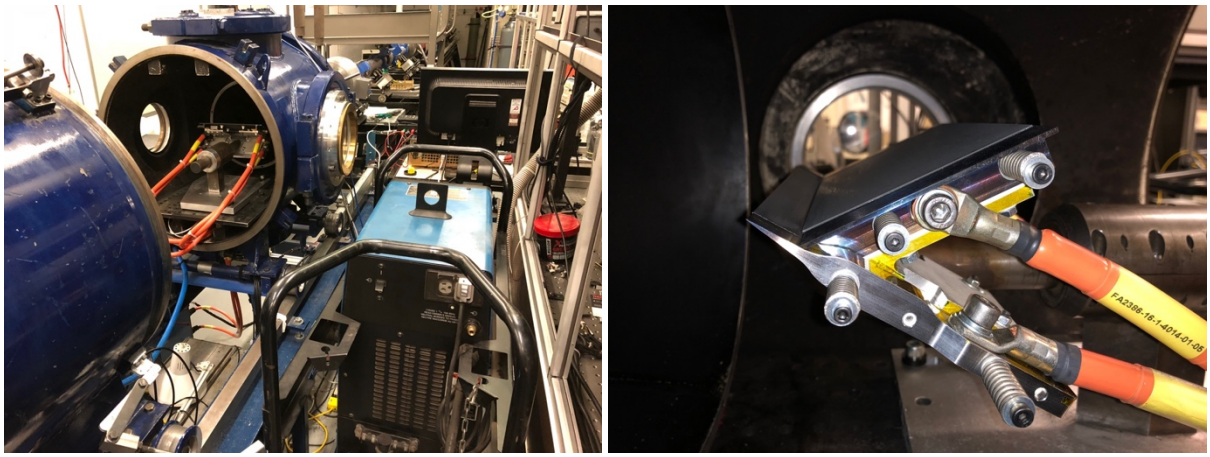

Figure 27. Heated tick model mounted in the T-ADFA test section.

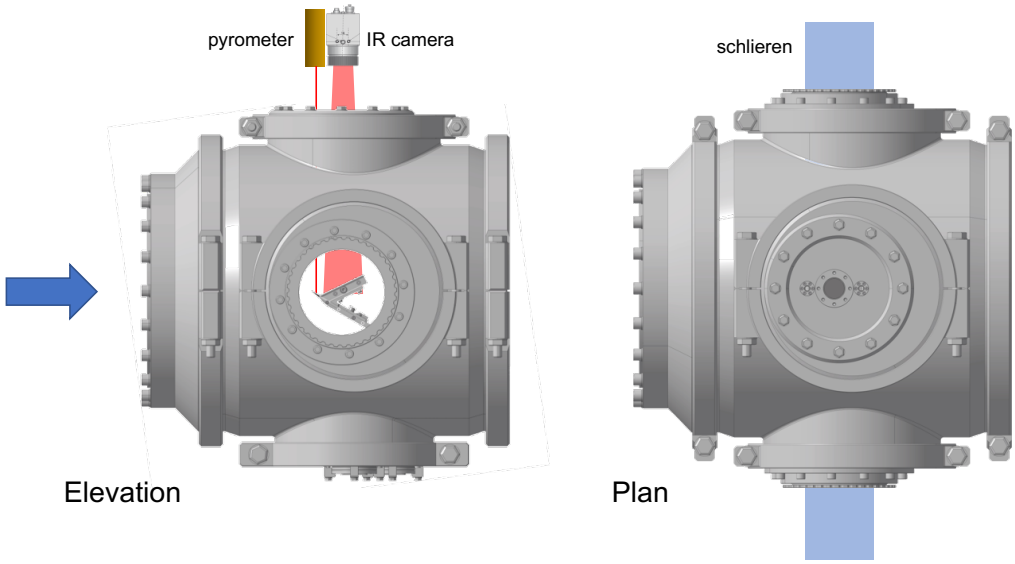

Figure 28. Figure of instrumentation set up.

Power was supplied to the expansion surface and compression surface circuits by two Miller Dynasty 350 welding power supplies (Figure 29). The supply for the compression surface heater was run at full power while the supply for the smaller expansion surface was run at a reduced power to match the surface temperature of the compression surface.

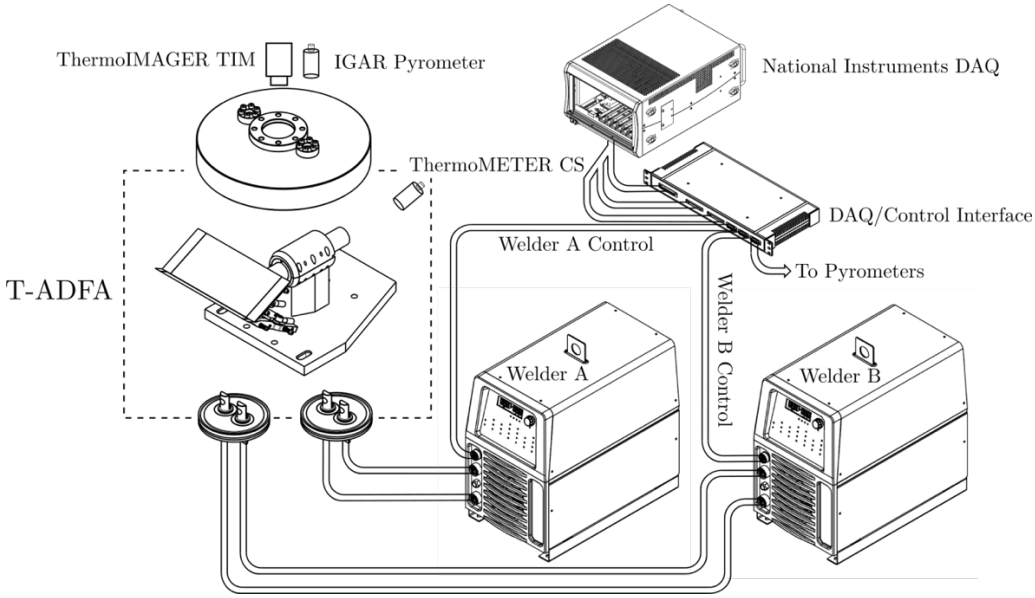

Figure 29. Instrumentation and control set up for heated tick experiment.

The graphite heater plates on the expansion and compression surfaces were both energised before the shot for the same duration (180 s) to bring them both up to their radiation adiabatic wall temperatures of approximately 800 K. The shock tunnel was then fired a few seconds before the end of the heating window, exposing the heated model to ~ 1ms of Mach 10 test flow. Power to the heaters was then automatically cut after the test flow. The operation sequence is shown in Figure 30.

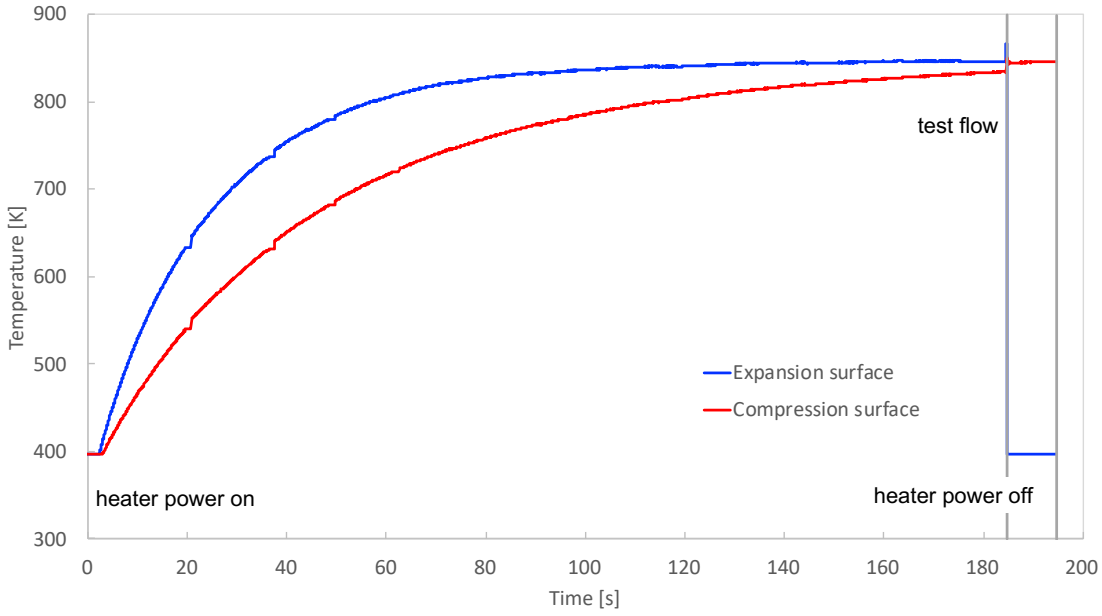

Figure 30. Experiment operation sequence (shown for Run2561)

The temperature distributions across the expansion surface and compression surface heaters were captured using the IR camera through the germanium window. An example temperature distribution from R2561, immediately preceding the flow arrival, is shown in Figure 31.

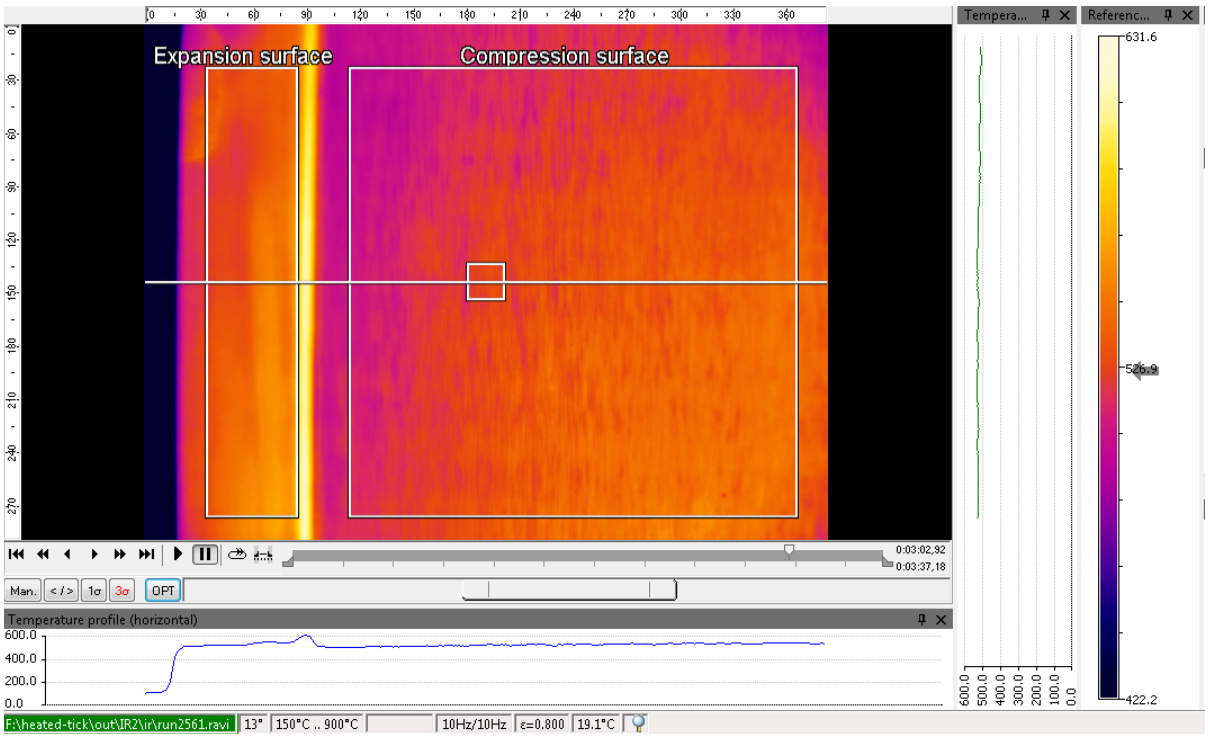

Figure 31. Temperature distribution from R2561, immediately preceding flow arrival.

Experimental Campaign

In the initial heated wall campaign, four hypersonic flow experiments were performed in the T-ADFA shock tunnel at a range of wall temperatures and thus wall-to-stagnation temperature ratios. All of the experiments were performed using the low-enthalpy condition E. The Nozzle reservoir and free-stream conditions for T-ADFA condition E are shown in Table 2. Nozzle reservoir and free-stream conditions for T-ADFA condition E (Park *et al.* 2010).

Table 2. Nozzle reservoir and free-stream conditions for T-ADFA condition E (Park *et al.* 2010)

p_o (MPa)	h_o (MJ.kg^{-1})	T_o (K)	M_∞	Re_∞ (m^{-1})	U_∞ (m.s^{-1})	p_∞ (Pa)	T_∞ (K)	ρ_∞ (kg.m^{-3})
11.3	3.1	3150	9.66	1.34 x10^6	2503	288.9	165	0.006

Pitot pressure histories (Figure 32) and core flow surveys (Figure 33) were measured by Kaseman (2017) during his cold wall experiments on the tick geometry using an earlier model. This shows that a large nominally two-dimensional region of flow can be expected over the middle of the tick model.

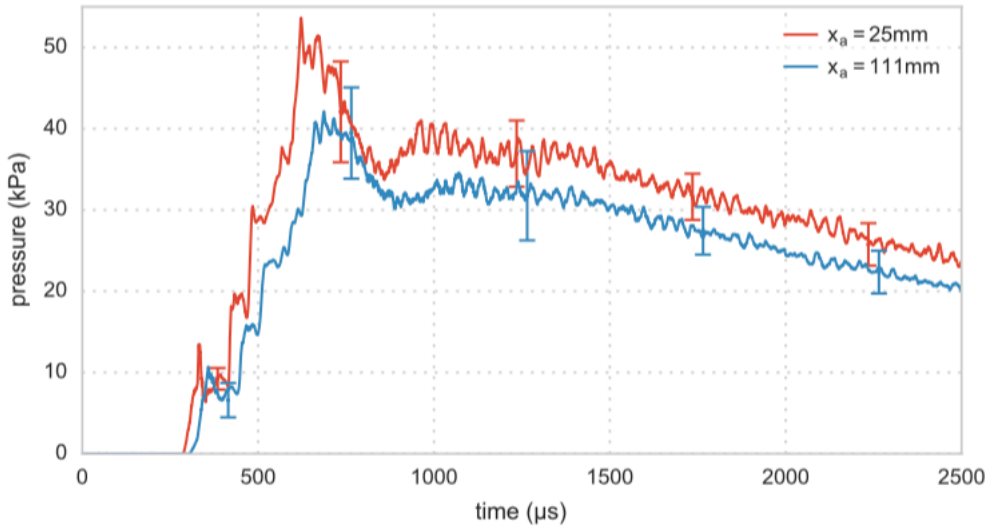

Figure 32. Condition E core flow pitot pressures at x_a = 25 mm and 111 mm. Error bars indicate the standard deviation in the pressure (Kaseman 2017).

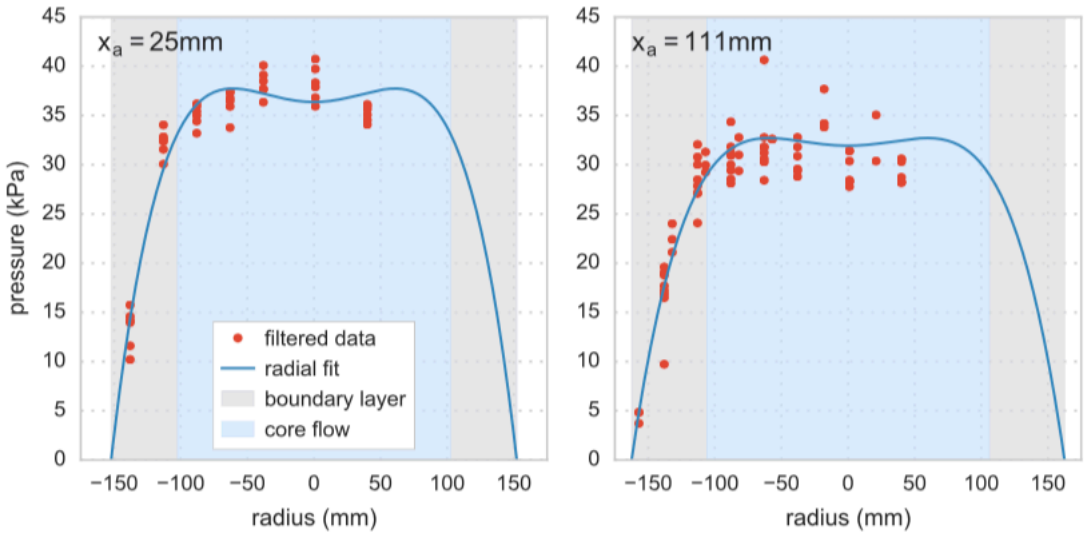

Figure 33. Condition E radial pitot pressure distribution at test time for the x_a = 25mm and 111 mm pitot survey locations (Kaseman 2017).

The individual runs performed in the current campaign are summarised in Table 3. The model proved prone to damage from impacts by diaphragm debris. The highly-stressed (aerodynamically and thermally) expansion surface, which formed the leading edge of the model, catastrophically failed after each of these impacts, ending the useful experiment. Sometimes the debris impacted the compression surface downstream, also damaging it. The model was therefore rebuilt between each tunnel run, replacing any damaged components. .

Table 3. Shock Tunnel Experiments

Run#	Condition	Heated	LE	Wall temperatures [K]		Temp Ratio	Flow Duration	Termination
				Expansion	Compression		[micro secs]	
R2561	E	Y	graphite	813	809	0.25	~600	end of test window
R2562	E	Y	graphite	720	747	0.23	467	impact on leading edge
R2563	E	N	graphite	295	295	0.09	333	impact on leading edge
R2564	E	N	steel	295	295	0.09	~600	end of test window

Results

Surface data

Figure 29 and Figure 30 show the predicted surface pressure and heat flux for the cold and heated wall temperatures (Tw = 300 K and 800 K, respectively). Effect of bluntness is shown in the figures for the cold wall case, considering a sharp leading edge case with a radius, r, ≤ 30 μm, and r = 100 μm as in the experiments. In the heated wall case, only the sharp leading edge case was considered at the time of the experiments. Due to manufacturing limitations on graphite, a minimum bluntness of r = 100 μm could be achieved. It should be pointed out that these simulations were carried out using the Navier-Stokes solver, US3D, and the solutions are steady state solutions. In the figures, the square symbol indicate flow reattachment for each case. The figures hence are meant to present an overall picture of the effect of wall heating and increased bluntness seen in the experiments. Based on the cold wall simulation, it can be seen that the increased bluntness from sharp to 100 μm pushes reattachment downstream by ~19%, while increased wall temperature from 300 K to 800 K has a lesser effect on reattachment, which showed only a ~10% downstream movement. It can be therefore expected that the increased bluntness in the experimental model to have a similar effect on reattachment. The reattachment and peak pressures due to the increased leading edge bluntness can also be expected to be higher compared to the sharp leading edge, while the peak heat flux (Figure 30) is expected to be less.

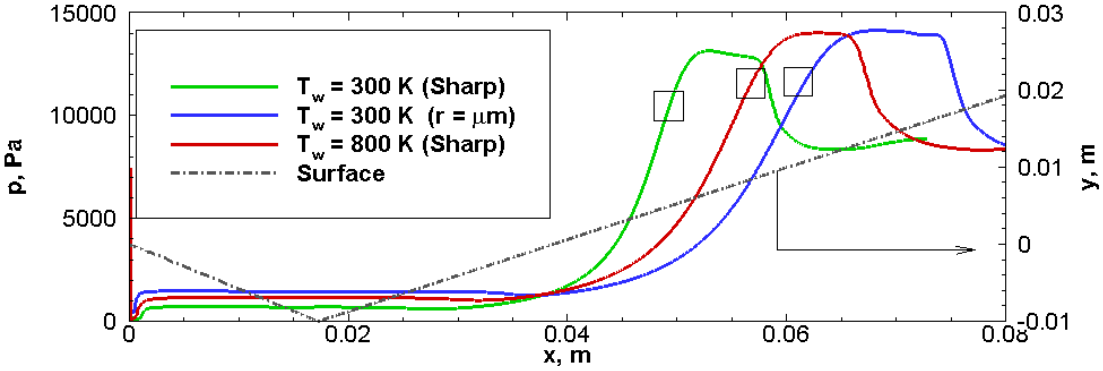

Figure 34. Predicted surface pressures.

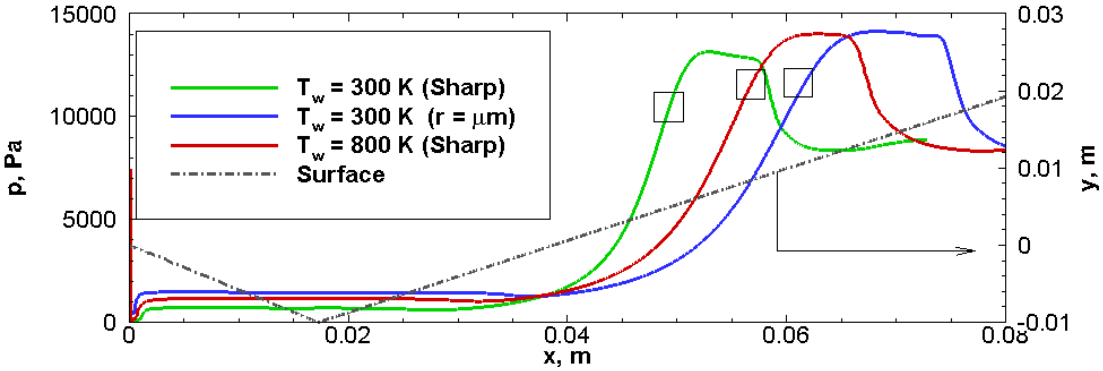

Figure 35. Predicted surface heat flux.

Cold wall (r = 100 µm)

Comparison is made below between the density gradient images obtained on the current model using shearing interferometry, run cold (Figure 36), and the predicted flow field from CFD (Figure 37).

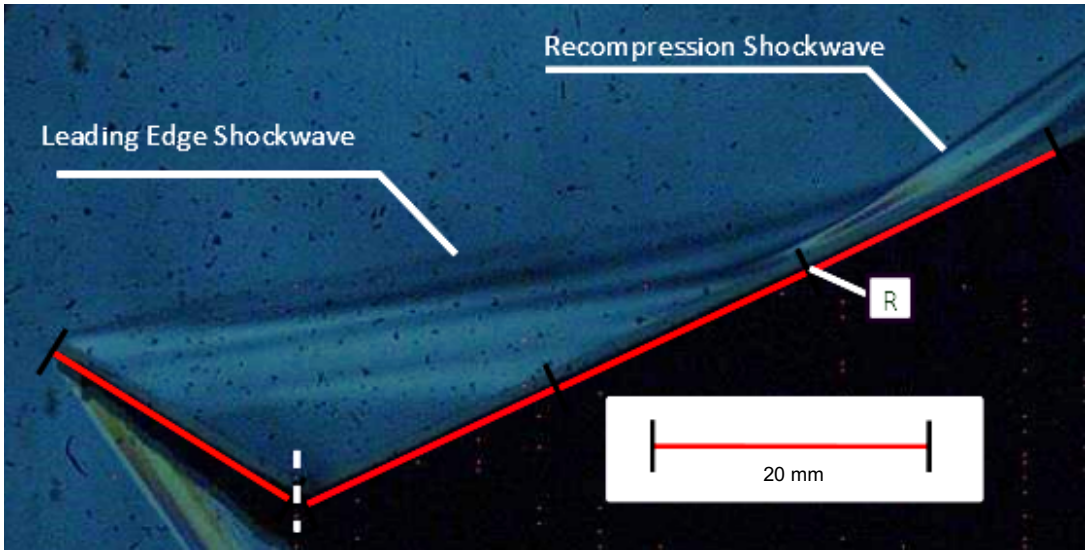

Figure 36. Density gradient image for Cold wall (r = 100 µm): run2564 (frame 013)

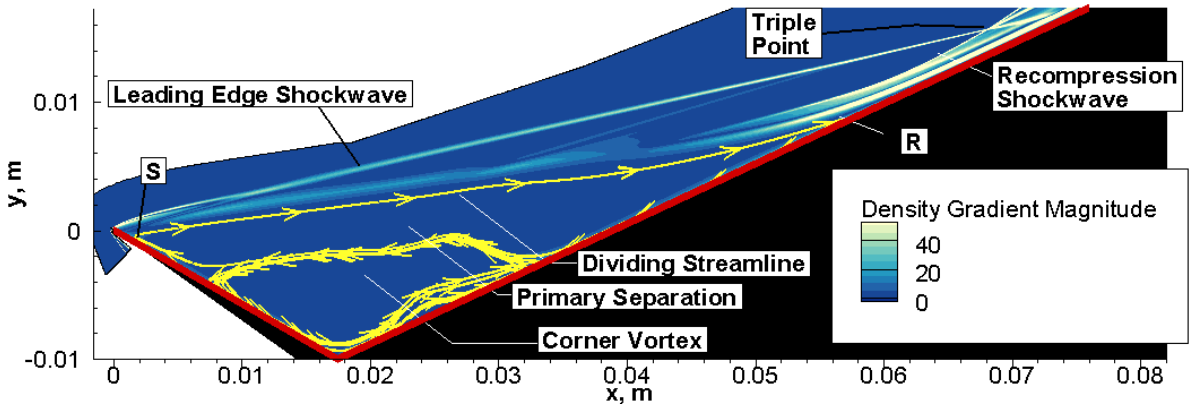

Figure 37. Cold wall (r = 100 µm): Density gradient magnitude from CFD.

Further comparison between (a) the flow visualisation on the current model (scaled appropriatel) and (b) the measured flow field from PLIF and that predicted flow field from CFD is also shown in Figure 38.

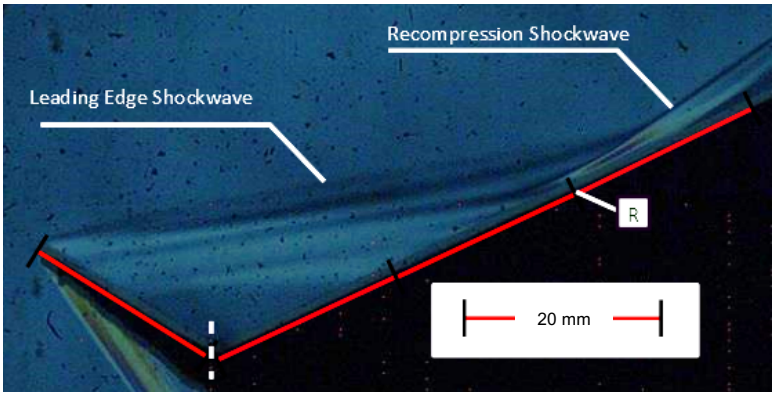

(a)

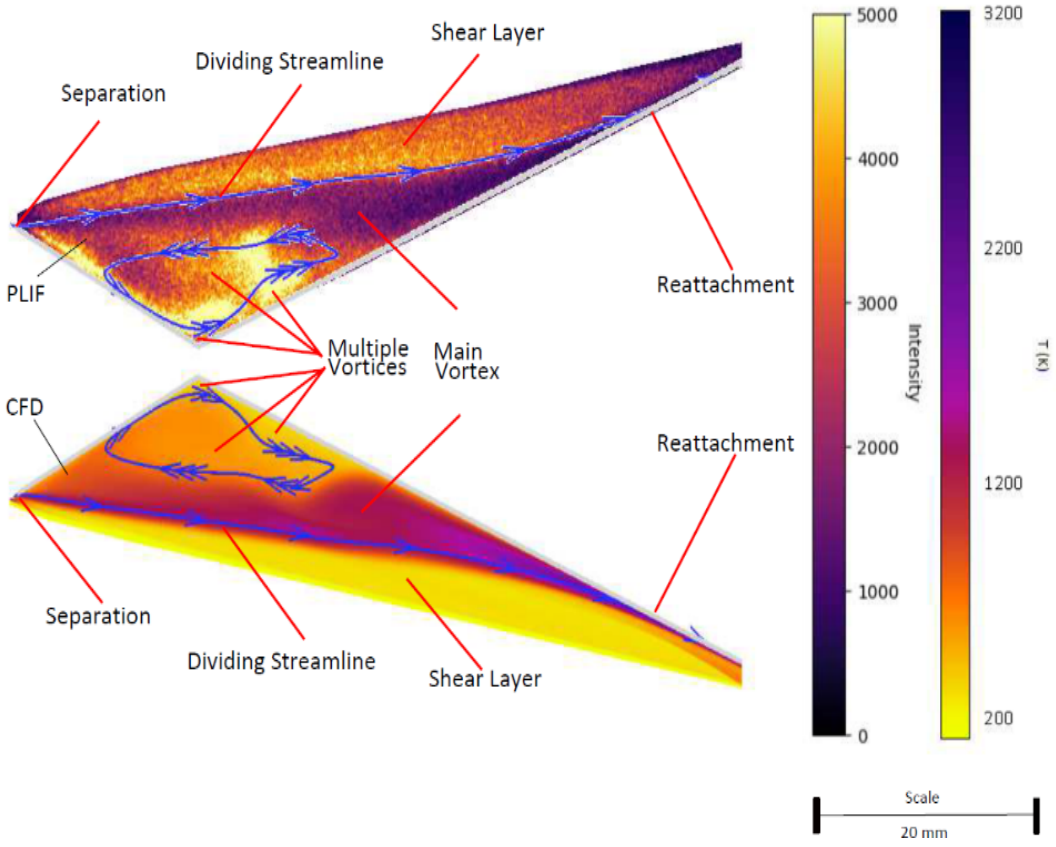

(b)

Figure 38. Cold wall (r = 100 μm): (a) density gradient image, (b) PLIF and CFD.

Hot wall (r = 100 µm)

Comparison is made below between the flow visualisation on the current model, run hot (Figure 38), and the predicted flow field for these conditions from CFD (Figure 37).

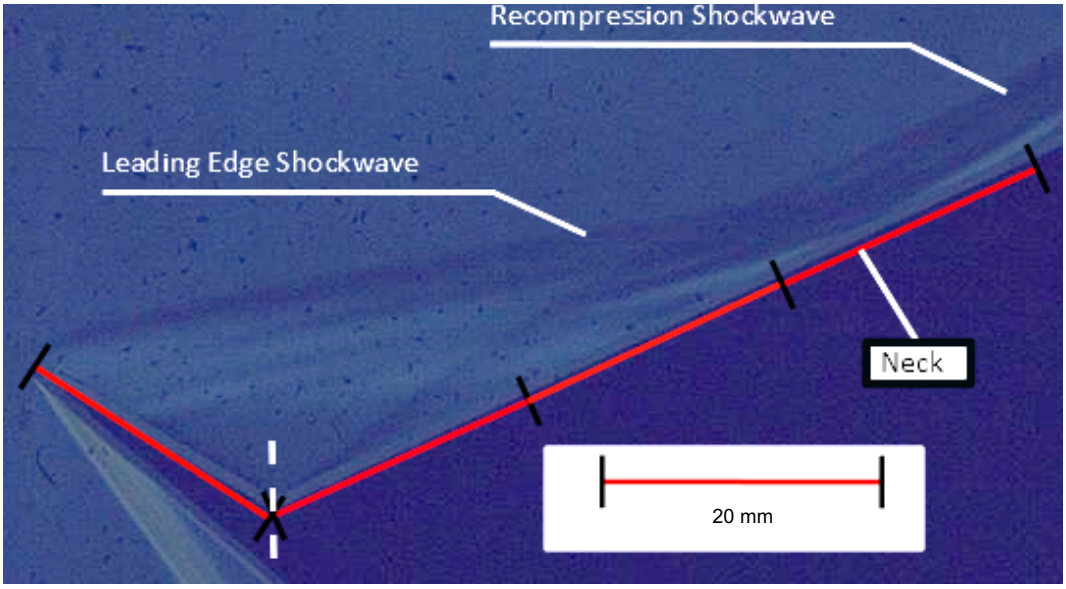

Figure 39. Density gradient image of Run2562, hot wall.

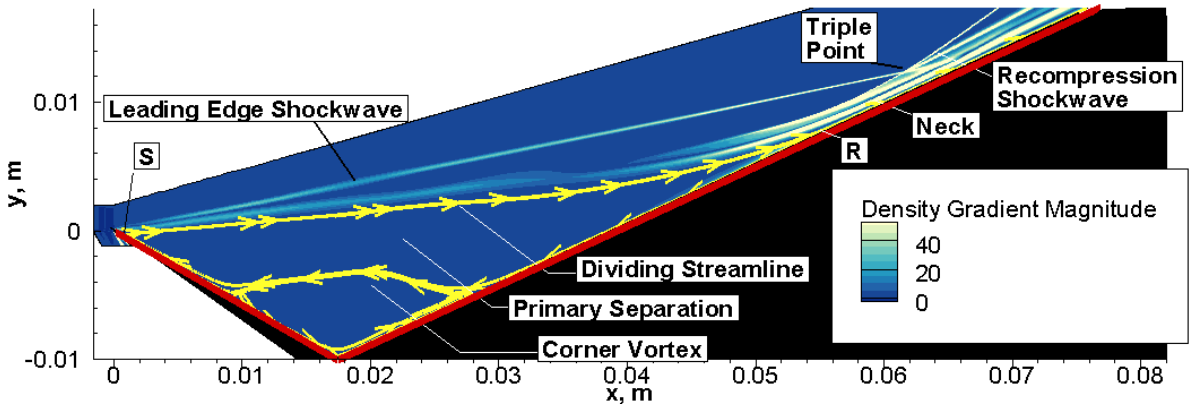

Figure 40. 800 K (r = 100 µm): Density gradient magnitude from CFD.

Conclusions and Recommendations

In this report, we have described experiments conducted on a large separated flow at hypersonic conditions in free-piston driven shock tunnel at an enthalpy of 3.1 MJ/kg, Reynolds number of 1.34 x 10^6 m^{-1} and a Mach number of 10. The unique feature of these experiments is that the model surface was heated up to 800K which yielded wall to stagnation temperature ratio of 0.25. The experimental model involved some unique design features including the use of graphite surface for heating.

Analysis and simulations, both Navier-Stokes and DSMC have shown that both primary and secondary separations are strongly influenced by the wall temperature. Our previous work has shown that the effect of wall heating can shift the centres of both primary and secondary vortices which, in turn, can have drastic effects when separation occurs on a control surface of a vehicle.

Experience gained from these experiments, which successfully demonstrated the design and implementation of complex and controllable hot wall models and showed reasonable agreement with numerical data, gives us

confidence that future work with higher wall temperatures is feasible using much simpler configurations such as a flat plate/ramp combination. Such a data would be of vital use to designers of future space vehicles.

References

Kaseman (2017) Optical studies of leading-edge separation in high-enthalpy, low-density hypersonic flows, UNSW PhD thesis.

Khraibut A, Gai S, Brown M, Neely A (2017) Laminar hypersonic leading edge separation – a numerical study, *Journal of Fluid Mechanics*, 821:624-646.

Kleine H (2001) Flow Visualization, ch. 5.2 in *Handbook of Shock Waves* vol. 1 (eds.: G. Ben Dor, O. Igra, T. Elperin), Academic, San Diego, pp.714-719.

Merzkirch W (1987) Flow Visualization, 2nd ed., Academic, Orlando, pp. 180-188

Neuer G, Jaroma-Weiland G (1998) Spectral and Total Emissivity of High-Temperature Materials, *International Journal of' Thermophysics*, Vol. 19, No. 3, pp. 917-929.

Prakash R, Gai S, O'Byrne S (2018). A direct simulation Monte Carlo study of hypersonic leading-edge separation with rarefaction effects. Physics of Fluids, 30(6), 063602.

Schnitzer M (2017) Development of Flat Plate Model with a resistively Heated Hot Wall and Leading Edge, Masters Thesis, Institute of Aerospace Thermodynamics, University of Stuttgart.

Tumuklu O, Levin DA (2017) On the temporal evolution in laminar separated boundary layer shock-interaction flows using DSMC. In 55th AIAA Aerospace Sciences Meeting.

Vennik J, Neely AJ, Tuttle T, Choudhury R, Buttsworth DR (2017) Reproducing Non-Uniform Surface Temperature Profiles on Hypersonic Cruise Vehicles in Impulsive Wind Tunnels, AIAA-2017-2194.